

Floor-Plan-aided Indoor Localization: Zero-Shot Learning Framework, Data Sets, and Prototype

Haiyao Yu, Changyang She, *Senior Member, IEEE*, Yunkai Hu, Geng Wang, Rui Wang, Branka Vucetic, *Life Fellow, IEEE*, and Yonghui Li, *Fellow, IEEE*

Abstract—Machine learning has been considered a promising approach for indoor localization. Nevertheless, the sample efficiency, scalability, and generalization ability remain open issues of implementing learning-based algorithms in practical systems. In this paper, we establish a zero-shot learning framework that does not need real-world measurements in a new communication environment. Specifically, a graph neural network that is scalable to the number of access points (APs) and mobile devices (MDs) is used for obtaining coarse locations of MDs. Based on the coarse locations, the floor-plan image between an MD and an AP is exploited to improve localization accuracy in a floor-plan-aided deep neural network. To further improve the generalization ability, we develop a synthetic data generator that provides synthetic data samples in different scenarios, where real-world samples are not available. We implement the framework in a prototype that estimates the locations of MDs. Experimental results show that our zero-shot learning method can reduce localization errors by around 30% to 55% compared with three baselines from the existing literature.

Index Terms—Indoor localization, zero-shot learning, graph neural networks, deep vision transformer.

I. INTRODUCTION

THE widespread adoption of the global navigation satellite system (GNSS) has revolutionized localization and navigation services, enabling the development of various applications in vertical industries and everyday life [1]. Although the GNSS can provide real-time localization with meter-level accuracy in most outdoor environments, it is not applicable in indoor environments due to signal blockage [2]. Nevertheless, there has been an increasing demand for indoor localization in different application scenarios, such as smart cities, intelligent plants, and Internet of Things (IoT) [3]. As an example, mobile users can quickly navigate to a specific store and get to the desired location with the indoor localization system.

The existing technologies for indoor localization [4] include wireless fidelity (WiFi) [5], Bluetooth [6], radio frequency identification device (RFID) [7], visible light [8], computer vision [9], magnetic field (MF) [10], pedestrian dead reckoning (PDR) [11], light detection and ranging (Lidar) [12], and ultra-wideband (UWB) [13]. Among them, visible light and Lidar

can achieve the highest positioning accuracy (centimeter-level) in scenarios with line-of-sight (LoS) paths. This fact limits its application in indoor localization, where LoS paths may not be available. The computer-vision-based techniques compare the captured images with pre-stored images to identify the location of the mobile device (MD) [14]. This approach is labor intensive as it needs image databases, and it raises potential issues on privacy. Both MF and PDR utilize the micro-electro-mechanical system (MEMS) technologies [15] that suffer from the accumulated errors [16]. For UWB and RFID, we need additional hardware to process the signals, and they are supported by limited cell phones [17, 18].

The primary demand for an indoor localization system is to choose a technology that is readily accessible at the user end. WiFi has stood out among these technologies due to its wide deployment in indoor environments. In particular, most electronic devices are WiFi-enabled, which makes WiFi an ideal candidate for indoor localization. Depending on the information available in WiFi systems, there are three types of information that can be used for indoor localization: 1) received signal strength (RSS)-based methods, 2) channel state information (CSI)-based methods, 3) and round trip time (RTT)-based methods.

From theoretical path-loss models, RSS can be converted into the propagation distance from an access point (AP) to an MD. Then, ranging-based methods, such as trilateration and least-square algorithm, are applied to estimate the location of the MD [4]. Due to the multi-path propagation of the signals, the accuracy of this approach highly depends on the propagation environment.

CSI is widely used in fingerprint-based localization algorithms. With this approach, we first need to collect the CSI of an MD in the considered area to construct an offline fingerprint data set. For real-time localization, the measured CSI of the MD is matched with the most similar CSI in the data set [3, 19–21]. Nevertheless, the fingerprint-based approach heavily relies on offline measurements and is highly sensitive to environmental changes.

In the IEEE 802.11-REVmc2, RTT protocol is available for estimating distances between MDs and APs [22]. The RTT protocol does not require clock synchronization between the MD and APs, and is applicable in dynamic communication environments with different types of devices [23, 24]. Nevertheless, in complex indoor environments with non-line-of-sight (nLoS) conditions, the RTT distance could be inaccurate due to multi-path propagation [25].

Although we can combine RTT, RSS, or CSI in localization

H. Yu, C. She, Y. Hu, G. Wang, R. Wang, B. Vucetic, and Y. Li are with the School of Electrical and Computer Engineering, University of Sydney, Sydney, NSW 2006, Australia.

E-mails: {haiyao.yu, changyang.she, yunkai.hu, geng.wang, r.wang, branka.vucetic, yonghui.li}@sydney.edu.au

The work of Changyang She was supported by the Australian Research Council (ARC) Discovery Early Career Researcher Award (DECRA) under Grant DE210100415. The work of Branka Vucetic was supported in part by the Australian Research Council Laureate Fellowship grant number FL160100032 and the Discovery Project grant number DP210103410.

[26, 27], these types of information may not be sufficient to achieve high localization accuracy. Other types of information are needed, especially in scenarios without LoS paths. For example, the results in [28] the geometric relationship among multiple clusters of users can be exploited to mitigate the nLoS effect. In [29], the environment information is integrated into the localization algorithm. Inspired by these works, we investigate how to exploit floor-plan images in localization algorithms. It's worth noting that floor-plan images can be readily obtained in most indoor scenarios, such as evacuation diagrams. The widespread use and mandatory updating of evacuation diagrams in most buildings ensure accessibility and up-to-date information of the floor plan. Please note that to estimate the location of an MD on a map, which is the floor-plan image in our work, we need to obtain the locations of APs through some simple measurements, which can be done very quickly.

A. Related Work

In LoS environments, the authors in [24] developed a clustering-based trilateration algorithm with the weighted concentric circle generation method, which demonstrates good tolerance and positioning accuracy. In [30], the authors utilized the weighted centroid and the particle swarm optimization algorithm to achieve a sub-meter positioning accuracy.

In mixed LoS/nLoS environments, most existing works first identify LoS and nLoS paths, and then calibrate the ranging errors. For example, in [31] and [32], Gaussian mixture models were established to identify nLoS RTT distances. Then, they are removed from the final estimation, and only LoS RTT distances will be preserved for localization. The authors in [33] applied the support vector machine (SVM) in the LoS/nLoS path classification, dividing the signals into high and low-quality ones. In [34], the authors proposed a convolutional neural network (CNN)-based LoS/nLoS path classification algorithm. In nLoS scenarios, another CNN-based regression algorithm was developed to estimate ranging errors. The authors of [35] further demonstrated that random forest surpasses SVM and deep neural network (DNN) in terms of the LoS/nLoS classification accuracy. With the help of the classification algorithms in [33–35], it is possible to achieve higher localization accuracy by removing nLoS paths from localization. Nevertheless, in the scenarios without a strong LoS path, improving the localization accuracy remains a challenging objective.

Deep learning has shown great potential in indoor localization. In [36], an unsupervised neural network was developed to improve the RTT ranging accuracy by learning the RTT patterns in different propagation environments. From the signals propagated in different mediums (e.g., metal, wood, etc.) and environments, a deep learning-based framework was proposed in [37] for estimating the propagation distance. The authors of [38] designed a hybrid CNN-based compensation distance network with a recurrent neural network (RNN)-based region proposal network to improve the accuracy of a fingerprint-based method. In scenarios with other types of sensors, the authors of [39] and [40] applied a factor graph to

integrate different types of information in indoor localization or navigation.

It is worth noting that most of the existing methods rely on labor-intensive and time-consuming measurements. Although with different training and testing data samples, the samples are collected in a single environment. Improving the generalization ability of learning-based localization algorithms in unseen environments with no or limited measurements deserves further study.

B. Contributions

This paper develops a floor-plan-aided indoor localization system that can achieve sub-meter-level accuracy in different indoor environments with mixed LoS and nLoS paths. The main contributions of this paper are summarized as follows:

- We establish a multi-user framework that consists of a graph neural network (GNN) and a floor-plan-aided deep neural network (FPDNN). By leveraging RTT distances and RSS, the GNN outputs the coarse locations of MDs. Then, the positioning accuracy is further improved by FPDNN, which utilizes the floor-plan image to acquire the signal propagation information in scenarios with mixed LoS and nLoS paths. With the RTT distances and RSS between MDs, our approach can estimate the locations of MDs that do not have stable connections with three or more APs.
- To improve the sample efficiency in a real-world environment, we build a virtual environment for synthetic data generation. With the help of synthetic data, the GNN and FPDNN are first pre-trained in the virtual environment and then deployed in the real-world environment. To apply the GNN and FPDNN in an unseen real-world environment with no data samples, we only need the floor-plan image to update the virtual environment. This can help to reduce labor and time consumption for measurement in the new environment. If some data samples are available, we can further increase the accuracy of our localization algorithm by fine-tuning the GNN and FPDNN in the new environment.
- To collect data samples and to evaluate the proposed localization algorithm, we develop a prototype and deploy it in three different environments: office, laboratory, and shopping mall. We collect around 100,000 samples in total. In each environment, the RTT distances and RSS from the MDs to all the APs are updated to our server in real-time, and the locations of MDs can be updated every 200 ms.
- Our field experiments show that the proposed framework can achieve sub-meter-level accuracy in environments with mixed LoS and nLoS conditions. Specifically, the root mean square error (RMSE) in the office, laboratory, and shopping mall are 0.87 m, 1.14 m, and 0.9 m, respectively. With our zero-shot learning approaches, the RMSE is around 30% \sim 55% lower than the baselines in [26], [41] and [24].

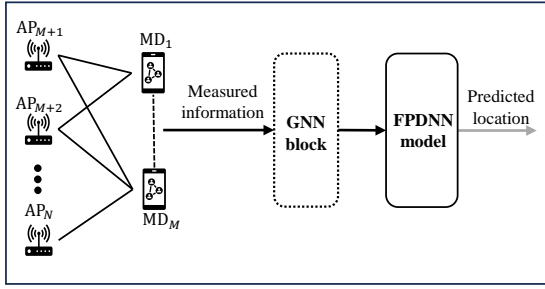


Fig. 1. Framework of the localization system.

C. Notations

In this paper, we use uppercase letters, e.g., X , to represent given constant numbers or parameters. Lowercase letters, e.g., x , are used to represent scalar variables. We use a calligraphic uppercase letter, e.g., \mathcal{A} , to denote a set, and $|\mathcal{A}|$ is its cardinality. In particular, $\{x_k\}_{k=1}^K$ denotes a set with given elements, i.e., $\{x_k\}_{k=1}^K = \{x_1, \dots, x_K\}$, and \mathbb{R} is the set of real numbers. We use an uppercase bold letter, e.g., \mathbf{A} , to represent a matrix, and a lowercase bold letter, e.g., \mathbf{a} , to denote a row vector. Superscript \top denotes the transposition of a matrix or vector, e.g., \mathbf{A}^\top and \mathbf{a}^\top , respectively. For matrices \mathbf{A} and \mathbf{B} , we define $[\mathbf{A}, \mathbf{B}]$ as their horizontal concatenation, while $\begin{bmatrix} \mathbf{A} \\ \mathbf{B} \end{bmatrix} = [\mathbf{A}^\top, \mathbf{B}^\top]^\top$ is the vertical concatenation. Other notations will be specifically stated.

II. FRAMEWORK OF LOCALIZATION SYSTEM

In this section, we elaborate on the framework of our proposed localization system. As depicted in Fig. 1, there are two blocks in the proposed framework: 1) the graph-based pre-localization, and 2) FPDNN for improving the localization accuracy. Details of these blocks will be elaborated in subsequent sections.

We consider a localization system with M MDs and K WiFi APs. Thus, there are a total of $N = M + K$ nodes in the network. The indices of MDs are denoted by $m \in \mathcal{M}$, where $\mathcal{M} \triangleq \{1, \dots, M\}$, and the indices of APs are denoted by $k \in \mathcal{K}$, where $\mathcal{K} \triangleq \{M + 1, \dots, M + K\}$. In some cases where we do not need to distinguish MDs and APs, we will use index n to refer to the n -th node.

Time is discretized into time intervals. In each time interval, an MD scans the nearby nodes (including both APs and MDs) and broadcasts the initial RTT request. The nodes respond to the request and send the acknowledgment back to the MD to establish the connection. Once the connection is established, the MD starts measuring the distance to nearby nodes, including MDs and APs [25]. The measurement between the m -th MD and the n -th node includes their RTT distance, $\zeta_{m,n}^{(t)}$, RSS, $\gamma_{m,n}^{(t)}$, and the index of the node. Thus, the information obtained by the m -th MD is given by

$$\mathbf{p}_{m,n}^{(t)} = [\zeta_{m,n}^{(t)}, \gamma_{m,n}^{(t)}, n], n \neq m. \quad (1)$$

Since an MD cannot establish a link to itself, we define $\mathbf{p}_{m,m}^{(t)} = \emptyset$.

In the t -th time interval, all the MDs upload their information to a server. The information that can be used for localization is denoted by $\mathbf{P}^{(t)}$, where

$$\mathbf{P}^{(t)} = \begin{bmatrix} \mathbf{p}_{1,1}^{(t)} & \mathbf{p}_{2,1}^{(t)} & \cdots & \mathbf{p}_{m,1}^{(t)} & \cdots & \mathbf{p}_{M,1}^{(t)} \\ \mathbf{p}_{1,2}^{(t)} & \mathbf{p}_{2,2}^{(t)} & \cdots & \mathbf{p}_{m,2}^{(t)} & \cdots & \mathbf{p}_{M,2}^{(t)} \\ \vdots & \vdots & \cdots & \vdots & \ddots & \vdots \\ \mathbf{p}_{1,N}^{(t)} & \mathbf{p}_{2,N}^{(t)} & \cdots & \mathbf{p}_{m,N}^{(t)} & \cdots & \mathbf{p}_{M,N}^{(t)} \end{bmatrix}. \quad (2)$$

From $\mathbf{P}^{(t)}$, the GNN estimates the coarse locations of MDs. Based on the coarse locations, the floor-plan image from each AP to the m -th MD is cropped from the floor-plan image, which is exploited by FPDNN to further improve localization accuracy. We note that the coarse locations obtained from the GNN help FPDNN to identify the communication environment between the MD and its neighbors. Thus, a better pre-localization algorithm helps to improve the final localization accuracy.

III. GNN PRE-LOCALIZATION

In this section, we first introduce how to construct a graph representation of a wireless network. Then, we develop a GNN for pre-localization to get the coarse locations of MDs.

A. Graph Representation

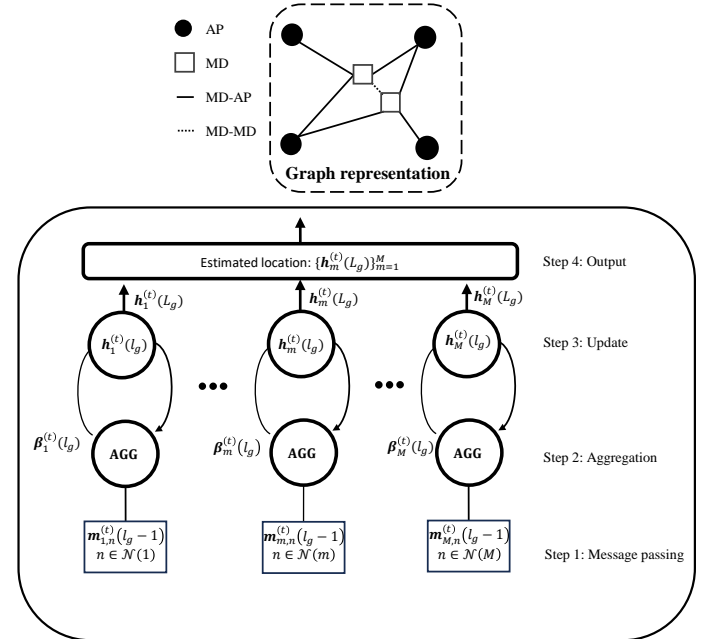


Fig. 2. Structure of GNN.

We denote the graph representation at the t -th time interval by $\mathcal{G}^{(t)}$. As depicted in Fig. 2, the circles are the APs, and the squares are the MDs. Each solid line is an edge between an MD and an AP, and the dashed line represents the edge between two MDs. The node and edge features are summarized as follows:

- The node feature of an AP is the coordinate of it,

$$\Upsilon_k = (x_k, y_k), k = M + 1, M + 2, \dots, N,$$

which remain constant in the localization system.

- The node feature of an MD includes the estimated location of it. The estimated location is updated by a GNN with L_g layers. We denote the edge feature in the l_g -th layer of the GNN by $\mathbf{h}_m^{(l_g)} \in \mathbb{R}^{2 \times 1}$. The initial node feature $\mathbf{h}_m^{(0)}$ is the estimated location obtained from the trilateration method that only exploits the RTT distances, $\zeta_{m,n}^{(t)}$.
- Let $\mathcal{K}_m^{(t)}$ and $\mathcal{M}_m^{(t)}$ be the sets of APs and MDs that can establish stable connections with the m -th MD at the t -th time interval, respectively. The set of neighbor nodes of the m -th MD is defined as $\mathcal{N}_m \triangleq \mathcal{K}_m^{(t)} \cup \mathcal{M}_m^{(t)}$. The edge feature between the m -th MD and the n -th node is defined as

$$\mathbf{e}_{m,n}^{(t)} = [\zeta_{m,n}^{(t)}, \gamma_{m,n}^{(t)}, n], \forall n \in \mathcal{N}_m.$$

We assume that two MDs can establish a stable connection between them when there is a LoS path. In nLoS cases, there is no edge between two MDs.

B. Graph Neural Network

The GNN is employed for the pre-localization of MDs. The input of the GNN block is the initial graph representation at the t -th time interval, $\mathcal{G}^{(t)}$. The output of the GNN block is the coarse locations of MDs, $\tilde{\Upsilon}_m^{(t)} = (\tilde{x}_m, \tilde{y}_m)^{(t)}$, $m = 1, 2, \dots, M$.

As shown in Fig. 2, the GNN consists of four steps: 1) message-passing, 2) aggregation, 3) feature update, and 4) output.

- 1) Message-passing: The GNN consists of L_g layers. The input of the m -th MD is $\mathbf{h}_m^{(0)}$, which is also the initial feature of the MD. In the l_g -th layer of the GNN, to update the feature of the m -th MD, all its neighbor nodes generate messages based on their features, $\mathbf{h}_n^{(l_g-1)}$, and the edge feature between the m -th MD and the n -th node, $\mathbf{e}_{m,n}^{(t)}$, $n \in \mathcal{N}_m$. The message can be expressed as

$$\mathbf{m}_{m,n}^{(t)}(l_g) = \phi\left(\mathbf{h}_n^{(t)}(l_g-1), \mathbf{e}_{m,n}^{(t)}; \boldsymbol{\theta}_M\right), \quad (3)$$

where $\phi(\cdot; \boldsymbol{\theta}_M)$ represents an feed forward neural network (FFNN) with parameters $\boldsymbol{\theta}_M$.

- 2) Aggregation: The m -th MD aggregates the messages from all its neighbors to obtain aggregated information $\boldsymbol{\beta}_m^{(t)}(l_g)$. The aggregation can be expressed as

$$\boldsymbol{\beta}_m^{(t)}(l_g) = \text{AGG}\left(\mathbf{m}_{m,n}^{(t)}(l_g), n \in \mathcal{N}_m\right). \quad (4)$$

In our GNN, we set the aggregation function to the mean of all the messages.

- 3) Feature update: The m -th MD updates its feature by merging $\mathbf{h}_m^{(t)}(l_g-1)$ and $\boldsymbol{\beta}_m^{(t)}(l_g)$. The output of the l_g -th layer can be expressed as

$$\mathbf{h}_m^{(t)}(l_g) = \varphi\left(\mathbf{h}_m^{(t)}(l_g-1), \boldsymbol{\beta}_m^{(t)}(l_g); \boldsymbol{\theta}_F\right), \quad (5)$$

where $\varphi(\cdot; \boldsymbol{\theta}_F)$ is an FFNN with parameters $\boldsymbol{\theta}_F$.

- 4) Output: After L_g rounds of updates, we can obtain the output from all the nodes, $\{\mathbf{h}_m^{(t)}(L_g)\}_{m=1}^M$. The output

of the GNN is the estimated locations of all the MDs, $\tilde{\Upsilon}_m^{(t)} = \mathbf{h}_m^{(t)}(L_g)$, $m = 1, 2, \dots, M$.

To train the GNN, we use the ground truth locations of MDs as labels, and minimize the gap between labels and the outputs of the GNN, e.g.,

$$\mathcal{L}_{\text{GNN}}(\boldsymbol{\theta}_M, \boldsymbol{\theta}_F) = \mathbb{E}(\|\tilde{\Upsilon}_m^{(t)} - \Upsilon_m^{(t)}\|^2), \quad (6)$$

where $\Upsilon_m^{(t)} \triangleq (x_m^{(t)}, y_m^{(t)})$ is the ground truth of the location, and $\|\tilde{\Upsilon}_m^{(t)} - \Upsilon_m^{(t)}\|^2$ is the Euclidean distance between $\tilde{\Upsilon}_m^{(t)}$ and $\Upsilon_m^{(t)}$. With the loss function in Eq. (6), we can use stochastic gradient descent to train the parameters $\boldsymbol{\theta}_M$ and $\boldsymbol{\theta}_F$ of the GNN.

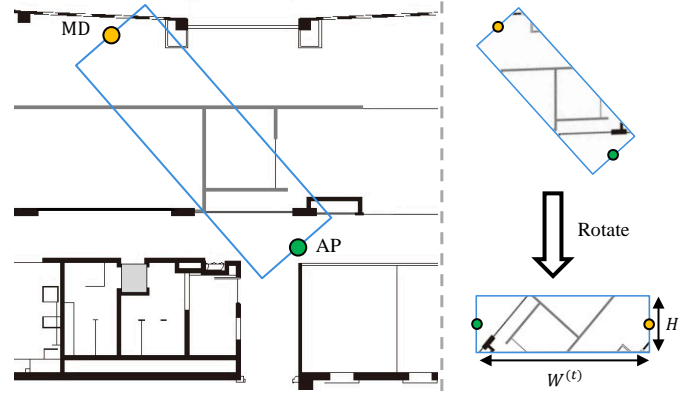


Fig. 3. Image preparation.

IV. FLOOR-PLAN-AIDED DEEP NEURAL NETWORK

In this section, we introduce FPDNN for a better estimation of the distance between an MD and an AP.

A. Image Preparation

As we mentioned, the RTT distance is biased due to the multi-path effect, especially when the LoS path is blocked. To improve localization accuracy, we utilize the floor-plan image between an MD and an AP. The images are cropped from the floor plan of the all area.

Fig. 3 shows the procedure for preparing images between the m -th MD and the k -th AP. We first find the coarse location of the MD estimated by the GNN block. Then, we crop a rectangular image with size $\{W^{(t)} \times H\}$ between the MD and the AP, where $W^{(t)}$ is the coarse distance between the MD and the AP, and H is the width of the image. It is worth noting that the selection of width H depends on the positioning accuracy of the coarse location. Specifically, the width H of the cropped image is set to 256, corresponding to approximately 4 m in the floor-plan image. The RMSE of the coarse location estimated by the GNN block is less than 2 m. Thus, the redundancy is sufficient for extracting geometric information surrounding the MD.

To regulate the cropped image, we rotate the image such that the direction from the AP to the MD in the image is always pointing rightward, as shown in Fig. 3. We denote the image

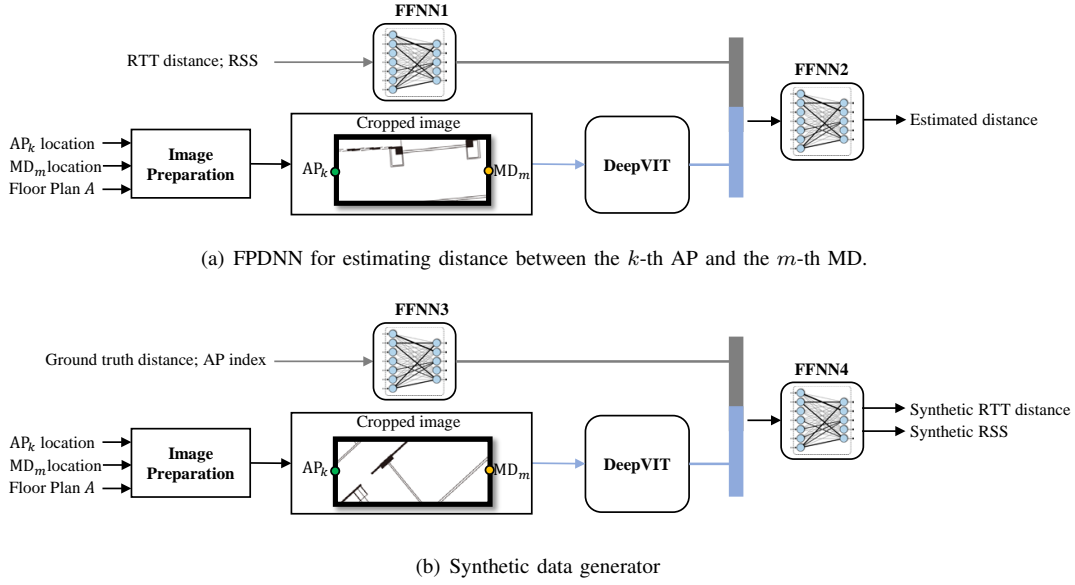


Fig. 4. Structure of FPDNN and synthetic data generator.

between the m -th MD and the k -th AP by $\mathbf{I}_{m,k}^{(t)} \in \mathbb{R}^{W^{(t)} \times H}$, which can be obtained from the following function,

$$\mathbf{I}_{m,k}^{(t)} = f_{IG}(\tilde{\Upsilon}_m^{(t)}, \Upsilon_k, \mathbf{A}), \quad (7)$$

where \mathbf{A} is the floor plan of the whole area, and $f_{IG}(\cdot, \cdot, \cdot)$ includes the image cropping and rotation.

Therefore, the input features of FPDNN include 1) the collected information from the MD, $\mathbf{P}_m^{(t)}$; 2) the images between the MD and its neighbor APs, $\{\mathbf{I}_{m,k}^{(t)}\} \forall k \in \mathcal{K}_m^{(t)}$.

B. Structure of FPDNN

In Fig. 4(a), we illustrate the structure of FPDNN and show how to estimate the distance between the m -th MD and the k -AP. FPDNN consists of three blocks: the deep vision transformer (DeepVIT) block and two FFNN blocks. At the t -th time interval, the image feature $\mathbf{I}_{m,k}^{(t)}$ and the measurement $\mathbf{p}_{m,k}^{(t)}$ are the inputs of the DeepVIT block and the first FFNN, respectively. The concatenation of their outputs serves as the input of the second FFNN, which outputs the estimated distance, denoted by $\hat{d}_{m,k}^{(t)}$. The true distance between the AP and the MD, denoted by $d_{m,k}^{(t)}$, is used as the label to train FPDNN.

The structures of the DeepVIT block and the two FFNNs will be further elaborated in the sequel.

1) *DeepVIT block*: DeepVIT is a kind of transformer that assigns weighting parameters to different parts of the image. The parts with higher weighting parameters will have stronger impacts on the final output. In this way, the output can “pay attention” to the important parts of the image.

The input of the DeepVIT block is the floor-plan image $\mathbf{I}_{m,k}^{(t)}$ and the output of the DeepVIT is the hidden feature given by \mathbf{o}_T . There are three different layers in the DeepVIT block, including the splitting and flattening layer, the position embedding layer, and the transformer encoder layer.

- *Splitting and flattening*: As shown in Fig. 5, the input image \mathbf{I} is split into $N_s^{(t)} = W^{(t)}H/P^2$ mini-images.

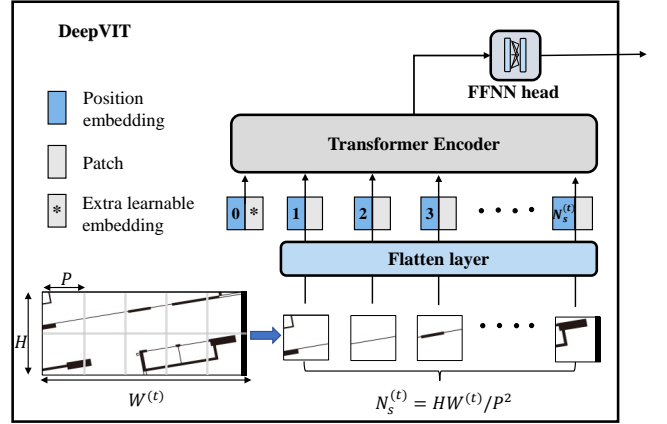


Fig. 5. Illustrate the structure of DeepVIT.

Let $\mathbf{I}_\ell \in \mathbb{R}^{P \times P}$ denote the ℓ -th mini-image, where P is the side length of each mini-image. Then, each mini-image is vectorized to a vector \mathbf{s}_ℓ with dimension $D' = P \times P$. For instance, let $\mathcal{I}_{i,j,k}$ denote the element of \mathbf{I}_ℓ at the position (i, j, k) , and then

$$\mathbf{s}_\ell = [\mathcal{I}_{1,1,1}, \mathcal{I}_{1,1,2}, \dots, \mathcal{I}_{1,1,C}, \mathcal{I}_{1,2,1}, \dots, \mathcal{I}_{1,P,C}, \mathcal{I}_{2,1,1}, \mathcal{I}_{2,1,2}, \dots, \mathcal{I}_{2,P,C}, \mathcal{I}_{3,1,1}, \dots, \mathcal{I}_{P,P,C}]. \quad (8)$$

Next, each vector \mathbf{s}_ℓ is compressed into the patch $\mathbf{s}_\ell \mathbf{E}$ with the size of $1 \times D$, where $\mathbf{E} \in \mathbb{R}^{D' \times D}$ denotes a trainable matrix. Finally, The output of the flatten layer, denoted as \mathbf{F} , is expressed as follows:

$$\mathbf{F} = \begin{bmatrix} \mathbf{s}_1 \mathbf{E} \\ \mathbf{s}_2 \mathbf{E} \\ \vdots \\ \mathbf{s}_{N_s} \mathbf{E} \end{bmatrix}, \quad (9)$$

where $\mathbf{F} \in \mathbb{R}^{N_s^{(t)} \times D}$.

- *Position embedding*: Following the approach in [42], an

extra learnable embedding $\mathbf{s}_{class} \in \mathbb{R}^{1 \times D}$ is prepended to \mathbf{F} , resulting in $\begin{bmatrix} \mathbf{s}_{class} \\ \mathbf{F} \end{bmatrix}$. Then, the position embedding, denoted as \mathbf{E}_{pos} , is applied to obtain the input of the transformer encoder, \mathbf{U}_T . Specifically,

$$\mathbf{U}_T = \begin{bmatrix} \mathbf{s}_{class} \\ \mathbf{F} \end{bmatrix} + \mathbf{E}_{pos}, \quad (10)$$

where $\mathbf{E}_{pos} \in \mathbb{R}^{(N_s^{(t)}+1) \times D}$. Please refer to [42] for more details on position embedding.

- *Transformer encoder*: The transformer encoder applied in this paper has the same structure as [43], which is comprised of two norm layers, a re-attention layer, and an FFNN head. It employs re-attention mechanisms to discern relationships among mini-images, thereby enhancing system performance. Given the input \mathbf{U}_T , the output of the transformer encoder can be expressed as

$$\mathbf{o}_T = f_T(\mathbf{U}_T; \boldsymbol{\theta}_T), \quad (11)$$

where f_T is a transformer encoder neural network, and $\boldsymbol{\theta}_T$ is the corresponding trainable parameters.

2) *FFNN layers*: The collected information $\mathbf{p}_{m,k}^{(t)}$ serves as input of the FFNN1. The first FFNN takes the measured information, $\mathbf{p}_{m,k}^{(t)}$, as its input and outputs some hidden features according to

$$\mathbf{o}_{F1} = f_{F1}(\mathbf{p}_{m,k}^{(t)}; \boldsymbol{\theta}_{F1}), \quad (12)$$

where $\boldsymbol{\theta}_{F1}$ are the training parameters.

The input of the second FFNN is $\mathbf{u}_{F2} = [\mathbf{o}_T, \mathbf{o}_{F1}]$. It outputs the estimated distance between the m -th MD and the k -th AP,

$$\hat{\zeta}_{m,k}^{(t)} = f_{F2}(\mathbf{u}_{F2}; \boldsymbol{\theta}_{F2}). \quad (13)$$

To train FPDNN, we use the ground truth distances between the m -th MD and the k -th AP $d_{m,k}^{(t)}$ as the labels. The loss function is defined as the mean square error (MSE) between the output of FPDNN and the label,

$$\mathcal{L}(\mathbf{E}, \boldsymbol{\theta}_T, \boldsymbol{\theta}_{F1}, \boldsymbol{\theta}_{F2}) = \mathbb{E}(\hat{\zeta}_{m,k}^{(t)} - d_{m,k}^{(t)})^2. \quad (14)$$

The parameters of FPDNN are updated by the stochastic gradient descent algorithm [44].

C. The Least Square Block

After obtaining the estimated distances from the m -th MD to all its neighbor APs, $\{\hat{\zeta}_{m,k}^{(t)}\}_{k \in \mathcal{K}_m^{(t)}}$, the least square algorithm is used to estimate the location of the MD [45]. The output of the least square can be expressed as

$$\hat{\Upsilon}_m^{(t)} = f^{LS}(\{\hat{\zeta}_{m,k}^{(t)}, \Upsilon_k\}_{k \in \mathcal{K}_m^{(t)}}), \quad (15)$$

where $f^{LS}(\cdot)$ is the least square algorithm, and $\hat{\Upsilon}_m^{(t)} \triangleq (\hat{x}_m, \hat{y}_m)^{(t)}$ is the location of the m -th MD.

In addition, the Kalman filter could be applied to improve the localization accuracy in the current time interval by using the historical trajectory of the MD.

V. SYNTHETIC DATA GENERATION IN VIRTUAL ENVIRONMENTS

The flow chart of pre-training is illustrated in Fig. 6. Considering that data samples in a real-world environment may not be enough for the training, we establish a virtual environment to generate synthetic data. In different real-world environments, the data samples may follow different distributions. The generator is first trained in the scenario 1 by the corresponding real-world data and floor-plan image. Then, the generator exploits floor-plan images in different target scenarios to generate synthetic data samples. The GNN and FPDNN are pre-trained offline using synthetic data samples. In this way, we can implement the localization algorithm in unseen environments without real-world data samples.

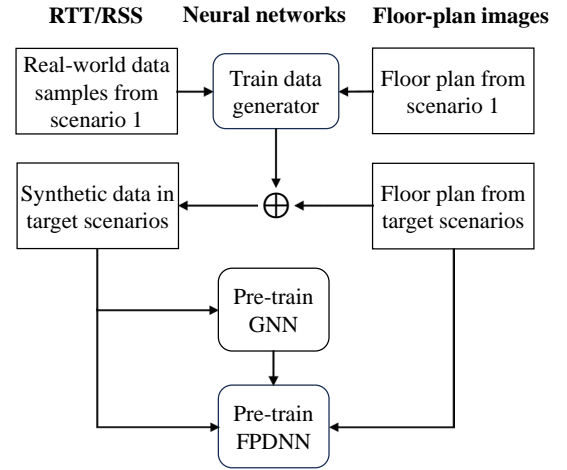


Fig. 6. Flow chart of the pre-training stage.

A. Synthetic Data Generation in One Virtual Environment

A data sample of our localization algorithm includes input information and the corresponding label. The input information of the t -th sample is composed of node and edge features of a graph, $\mathcal{G}^{(t)}$, and the floor-plan image between the MD and its nearby APs, $\mathbf{I}_{m,k}^{(t)}$. The label is the ground truth location of the MD, $\Upsilon_m^{(t)}$.

One way to generate synthetic data samples is to use commercial ray-tracing models [46]. The idea is to generate a set of locations of the m -th MD and estimate the RTT distance and RSS from each location to its neighbor nodes from ray-tracing models. There are three major issues that forbid the usage of ray-tracing models in our problem: 1) ray-tracing models are very sensitive to the dielectric properties of the reflective surfaces of the obstacles in the radio environment; 2) ray-tracing requires detailed three-dimensional (3D) geometric information; 3) the computing time for generating a sample in ray-tracking models is high, especially when there are a large number of paths between an MD and an AP.

Alternatively, we use a deep learning model to generate the RTT distance and RSS for a set of locations of the MD. Given the locations of the m -th MD and the k -th AP, we can obtain the ground-truth distance $d_{m,k}^{(t)}$ and the floor-plan image $\mathbf{I}_{m,k}^{(t)}$ between them. As shown in Fig. 4(b), the deep learning

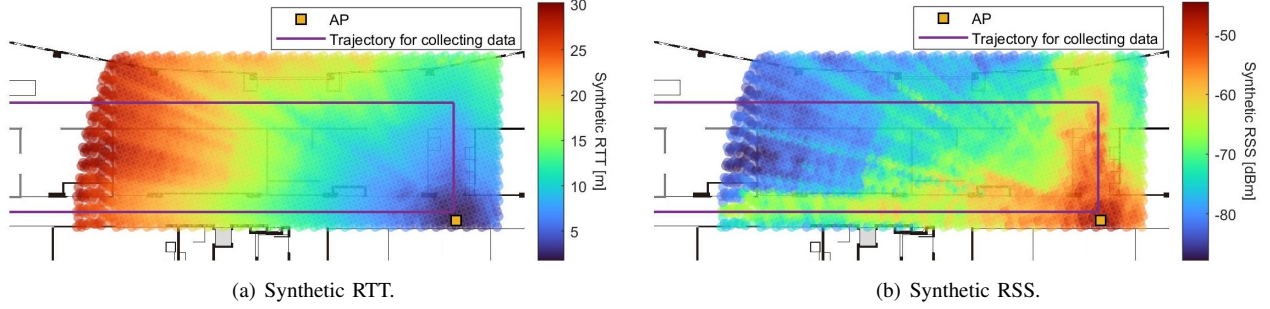


Fig. 7. Synthetic data generator in the office.

model is composed of two FFNNs and a DeepViT and can be expressed as

$$[\tilde{\zeta}_{m,k}^{(t)}, \tilde{\gamma}_{m,k}^{(t)}] = \phi_D(d_{m,k}^{(t)}, \mathbf{I}_{m,k}^{(t)}; \boldsymbol{\theta}_D), \quad (16)$$

where ϕ_D is a DNN in Fig. 4(b), and the corresponding training parameters are $\boldsymbol{\theta}_D$. The output $\tilde{\zeta}_{m,k}$ and $\tilde{\gamma}_{m,k}$ are the synthetic RTT distance and RSS, respectively.

The generator is trained in a supervised manner with the following loss function

$$\mathcal{L}(\boldsymbol{\theta}_D) = \mathbb{E}((\tilde{\zeta}_{m,k}^{(t)} - \zeta_{m,k}^{(t)})^2 + (\tilde{\gamma}_{m,k}^{(t)} - \gamma_{m,k}^{(t)})^2), \quad (17)$$

where $\zeta_{m,k}^{(t)}$ and $\gamma_{m,k}^{(t)}$ are the RTT distance and RSS of the same location in the real-world scenario. For example, to generate synthetic data in the office scenario in Fig. 7, we collected real-world data samples on the purple trajectory and then used them as labeled samples. After training, we used the synthetic data generator to estimate the RTT distance and RSS at any location in the office.

B. Synthetic Data Generation in Different Environments

In other environments, such as the shopping mall and laboratory, the corresponding floor-plan images are used to generate synthetic data samples. There is no need to fine-tune the synthetic data generator in new scenarios. Note that the motivation for using synthetic data is to improve the diversity of the training samples for our localization algorithm. The distribution of synthetic data samples in an unseen scenario does not need to be the same as the real-world data samples. The difference between them increases the diversity of data samples and may help improve the generalization ability of our localization algorithm.

VI. WiFi PLATFORM AND DATA SETS

In this section, we introduce the WiFi Platform and data sets in each scenario.

A. WiFi Platform

The WiFi platform consists of eight APs, two line-tracking vehicles, four mobile phones, and a laptop. The details of these devices are given as follows:

- *Access points*: As shown in Fig. 9, Google Nest WiFi APs, which support both 2.4 GHz and 5 GHz with IEEE 802.11 mc standard, are used in our platform. We note

that RTT and RSS are obtained from reference signals with carrier frequency at 5 GHz. In each of the three scenarios, the locations of all eight APs are fixed, and the heights of the tripods are 1.5 m.

- *Line-tracking vehicles*: Makeblock Ultimate 2.0 programmable robot kits are used to build line-tracking vehicles. The line-tracking vehicles are programmed to follow the black line at a constant speed. Each vehicle is equipped with two mobile phones. The horizontal mobile phones (C2 and C3 in Fig. 9) measure the RTT and RSS from nearby APs. The vertical mobile phones (C1 and C4 in Fig. 9) measure the RTT and RSS between each other.
- *Mobile phones*: The four mobile phones are either Google Pixel 6 Pro or Google Pixel 6a with Android 13. To measure the RTT and RSS between C1 and C4, we use WiFi NanScan, developed by Google. To measure the RTT and RSS from C2 or C3 to all the APs simultaneously, we developed an application ourselves because the available applications can only measure RTT and RSS from one AP to the mobile phone at a time. The sampling interval between the mobile phones and the APs is set to 200 ms, and the sampling interval between C1 and C4 is set to 1 s.
- *Server*: A desktop is used as a server. The detailed specifications for the server are Windows 11 Pro, Intel(R) Core(TM) i9-12900KF central processing unit (CPU) @ 3.20GHz, NVIDIA GeForce RTX 3090, 64GB Memory, and 1TB SSD.

B. Typical Scenarios

We collect our data sets in the following three scenarios on the campus of the University of Sydney. All these three scenarios mixed with both LoS and nLoS paths.

- *Office*: The data samples are collected in the office of the Center of IoT and Telecommunications. This area consists of one long office corridor and an office room, i.e., a $60 \times 20 \text{ m}^2$ rectangular area.
- *Laboratory*: The data samples are collected in the Mechanical Engineering Laboratory. The lab has multiple cement posts, iron guardrails, and an elevator, covering a $25 \times 9 \text{ m}^2$ rectangular area.
- *Shopping mall*: The data samples are collected in the shopping mall in the Wentworth building at the university



Fig. 8. Different environments and corresponding floor plans. Left: Office. Middle: Shopping mall. Right: Laboratory. The furniture is not included in the floor plans, and our evaluation results are obtained in real-world environments with furniture.

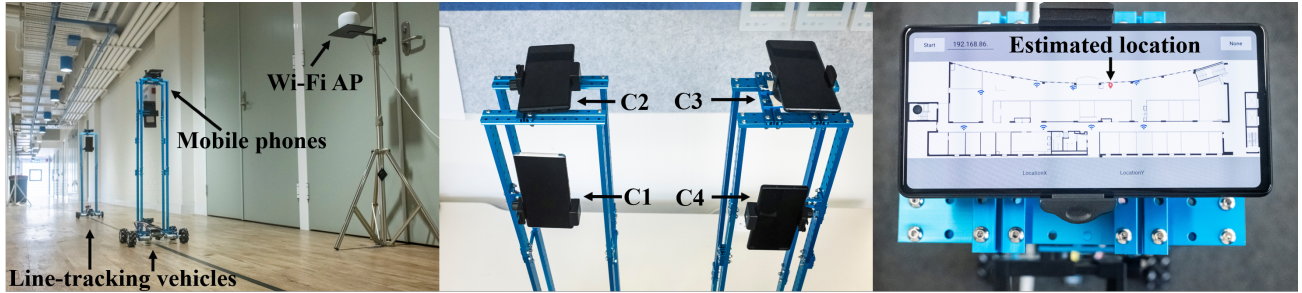


Fig. 9. Experiment setup. Left: Wi-Fi AP and line-tracking vehicles. Middle: Mobile devices. Right: estimated location of the MD on the map.

campus. The experiment is carried out in the mall hallway outside the shops, i.e., a bank, a chemist, and a coffee shop.

All the scenarios and their corresponding floor-plan images are provided in Fig. 8.

C. Data Sets

The data set¹ of each scenario consists of RTT distance, RSS, and floor-plan image.

1) *Data calibration and processing*: As introduced in [22], there are offset components between the RTT distance and the ground truth distance, which lead to inaccurate RTT measurement. These components are static and can be removed from the measured RTT distance. Specifically, we compare the true distance and the measured RTT distance between all the APs and the MD. The results show that the offset components lead to a nearly constant value between the real distance and the measured distance. Then, the average offset between the MD and each AP is removed from the raw RTT distance.

In our data sets, we provide the raw data as well as the data sets after calibration and processing. We note that since the heights of APs and MD are fixed, we convert the RTT

distance from in 3D space into a two-dimensional (2D) plane, which can be easily used in 2D localization algorithms. We also preserve the original RTT distance in the 3D space in our data sets.

2) *Illustration of data set*: As shown in Section VI-B, we collected our data samples in three scenarios. For each scenario, we created four files: 1) the floor plan of the scenario, 2) measured information from each mobile phone to all the APs, 3) measured information between C1 and C4, and 4) the locations and indices of the APs.

We take the “office” as an example to illustrate our data sets. The locations of all the APs, the trajectory of the vehicles, and the layout of the office can be found in Fig. 10. As shown in Table I, a sample between the MD and all APs consists of a time stamp, RTT distance, RSS, and the ground truth location of the MD.

D. Measurement Errors

1) *RSS measurement errors*: From the theoretical path-loss models of wireless channels, we can estimate the distance between two devices based on the RSS. The RSS could be inaccurate due to stochastic interference and noise. In addition, since the communication environment is dynamic, walls and obstacles may cause severe signal attenuation and

¹Available at: <https://github.com/haiyaoyu/RTT-Indoor-localization-data-set>

TABLE II
THE HYPER-PARAMETERS FOR THE GNN MODEL, FPDNN MODEL, AND DATA GENERATOR.

FPDNN				
Block	Layer	Input Shape	Output Shape	Remark
FFNN1	FC1	2	64	first fully-connected layer with Relu
	Norm	64	64	layer normalization
	FC2	64	32	second fully-connected layer with Relu and 0.2 dropout rate
Image Pre-processing	Image Splitting	$W^{(t)} \times 256 \times 1$	$N_s^{(t)} \times 32 \times 32$	$H = 256, C = 1, P = 32$
	Flattening	$N_s^{(t)} \times 32 \times 32$	$N_s^{(t)} \times 512$	$D' = 1024, D = 512$
	Position Embedding	$N_s^{(t)} \times 512$	$(N_s^{(t)} + 1) \times 512$	add extra learnable embedding
DeepVIT Transformer Encoder	Norm	$(N_s^{(t)} + 1) \times 512$	$(N_s^{(t)} + 1) \times 512$	layer normalization
	Re-attention	$(N_s^{(t)} + 1) \times 512$	$2 \times (N_s^{(t)}) \times 64$	number of attention heads: 2
	FC1	$2 \times (N_s^{(t)}) \times 64$	$N_s^{(t)} \times 512$	first fully-connected layer with Relu
	Norm	$N_s^{(t)} \times 512$	$N_s^{(t)} \times 512$	layer normalization
	FC2	$N_s^{(t)} \times 512$	$N_s^{(t)} \times 512$	a fully-connected layer with Gelu and 0.2 dropout rate
	mean	$N_s^{(t)} \times 512$	1×512	-
DeepVIT FFNN Head	Norm	1×512	1×512	layer normalization
	FC1	1×512	1×32	fully-connected layer with Relu
FFNN2	FC1	1×64	1×32	first fully-connected layer with Relu
	Norm	1×32	1×16	layer normalization
	FC2	1×16	1	second fully-connected layer with Relu
GNN				
Message-passing $\phi(\cdot; \theta)$	FC1	9	8	fully-connected layer with Relu
	FC2	8	2	second fully-connected layer
Aggregation	mean	2	2	-
Update $U(\cdot; \varphi)$	FC1	7	8	first fully-connected layer with Relu
	FC2	8	2	second fully-connected layer with Relu
DNN in Synthetic Data Generation				
FFNN4	FC1	64	32	first fully-connected layer with Relu
	Norm	32	32	layer normalization
	FC2	32	2	second fully-connected layer with Relu and 0.2 dropout rate

To train the synthetic data generator, we collect samples in the office. As shown in Fig. 10, a line-tracking robot moves along the trajectory (with legend ‘‘Trajectory’’) for five circles. We have 50,000 data samples in this scenario, and each data sample consists of the RTT and RSS information from an AP to the MD. We use the samples collected in the first four circles to train the data generator. After the training, the generator can output RTT and RSS information at any location in the office, as illustrated in Fig. 7.

E. Localization in The Office

1) *Training with real-world data samples:* We first evaluate the performance of our algorithm when it is trained with real-world data samples in the office environment. Specifically, we use 80% of the samples for training and the rest 20% of the samples for testing. The estimated locations using the hybrid RTT-RSS model in [26], Bayesian grid update model in [41], CbT+WCCG method in [24], and our proposed method, are shown in Fig. 11. The results indicate that the estimated locations of our method are well-aligned with the ground-truth trajectory in Fig. 10, and the localization errors are much lower than the other three baselines.

To further illustrate the localization errors of different methods, we provide the CDFs of localization errors in Fig. 12. With our algorithm, the median of localization errors is 0.2 m, and the localization errors are lower than 0.44 m with a probability of 90%. For the other three baselines, their medians are larger than 1.5 m, and the 90-th percentile CDFs are larger than 3 m.

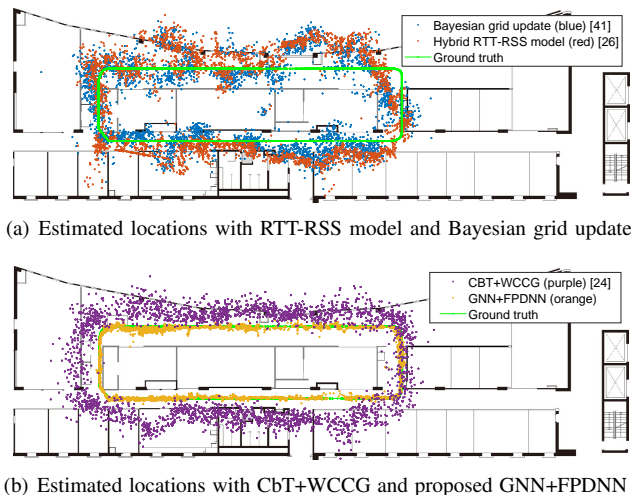


Fig. 11. Localization with our method (GNN+FPDNN) and three existing baselines.

2) *Zero-shot learning without real-world data samples:* In Figs. 13 and 14, GNN and FPDNN are trained with the synthetic data generator. To validate the effectiveness of our synthetic data generator, we changed the deployment of APs in testing. The locations of APs in Fig. 10 are different from the locations of APs in Fig. 15(a). Since there is no real-world sample in the new scenario, this approach is known as zero-shot learning.

The estimated locations in Fig. 13(a) are obtained with the GNN (either with or without Kalman Filter). With the help

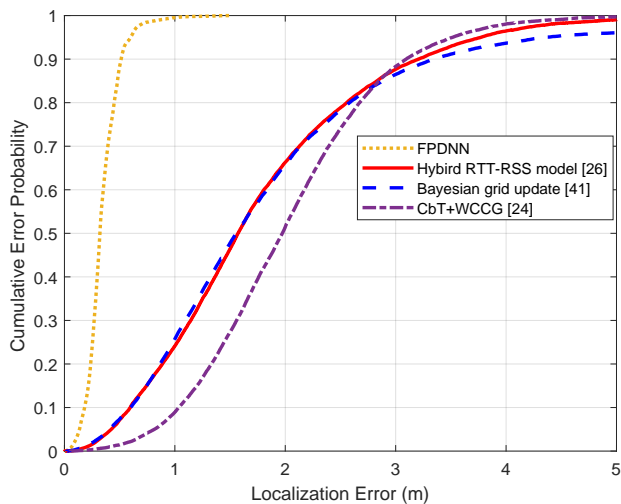


Fig. 12. CDFs of localization errors, where GNN and FPDNN are trained with real-world samples.

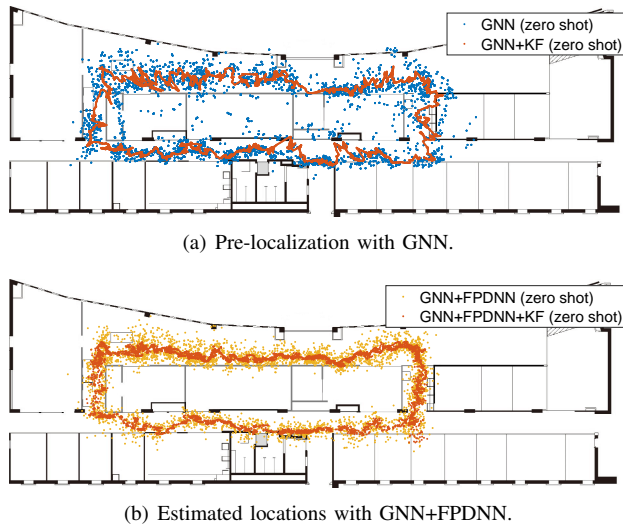


Fig. 13. Locations of APs, ground truth, and estimated locations.

of the Kalman Filter, we can obtain better pre-localization accuracy, and the corresponding results serve as one part of the input in the FPDNN. In Fig. 13(b), we show the final results obtained from the FPDNN. The results indicate that by combining the GNN, the FPDNN, and the Kalman filter, the estimated locations are close to the ground truth in Fig. 10. The RMSE of the estimated location with the GNN and Kalman filter is 1.33 m, and the location RMSE with the GNN+FPDNN is 1.15 m. After smoothing by the Kalman filter, the RMSE further decreases to 0.95 m.

The CDFs of the location errors are illustrated in Fig. 14. From the CDFs, the medians of localization errors achieved by the four approaches mentioned above are 0.82 m, 0.95 m, 1.05 m, and 1.26 m, respectively. With a probability of 90%, the estimation errors of the four approaches are lower than 1.39 m, 1.73 m, 2.06 m, and 2.46 m, respectively. By combining the GNN, the FPDNN, and the Kalman Filter, the RMSE is 0.95 m, even with no sample in the new scenario. These results indicate that with the help of synthetic data samples, our method outperforms the three existing baselines in unseen scenarios.

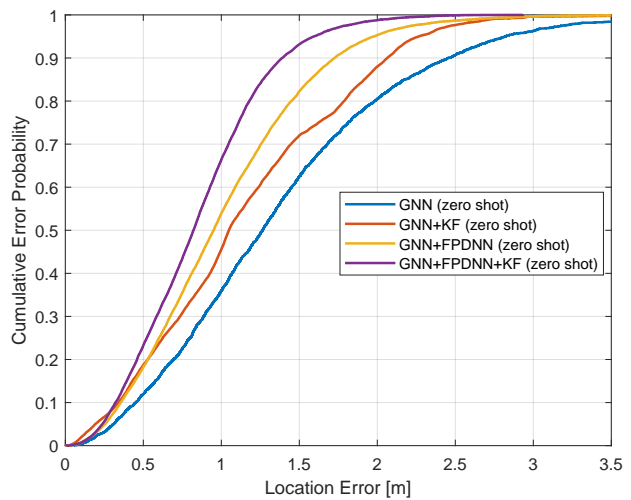


Fig. 14. CDFs of localization errors achieved by zero-shot learning approaches.

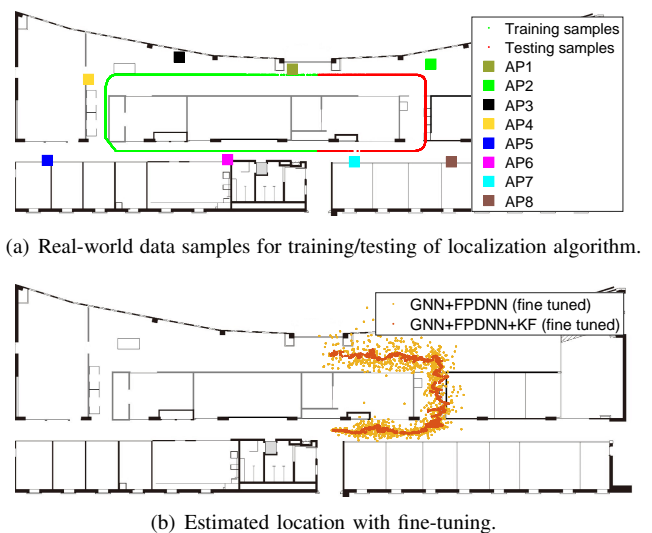
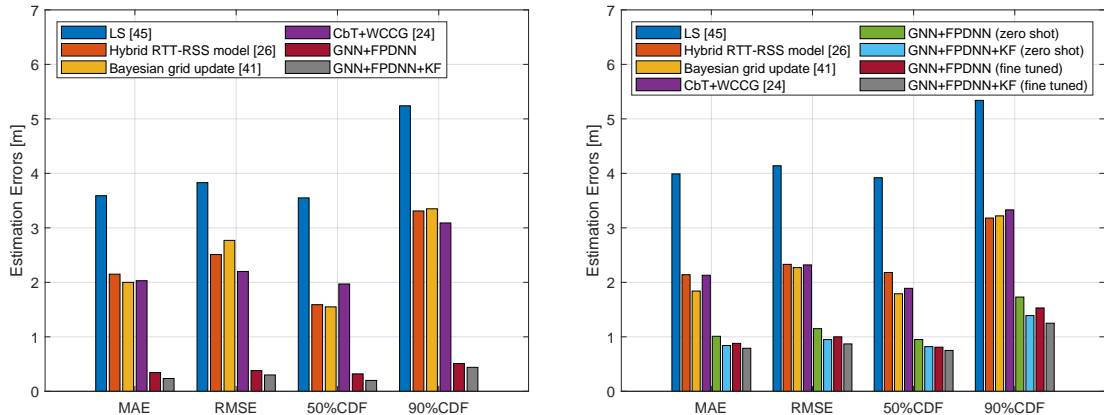


Fig. 15. Locations of APs, ground truth, and estimated locations.

3) *Fine-tuning with part of real-world data samples*: The localization accuracy can be further improved if parts of the real-world data samples are used to fine-tune the pre-trained GNN and FPDNN. As shown in Fig. 15(a), the samples used in fine-tuning and testing are in green and red, respectively. The testing results are shown in Fig. 15(b). To better illustrate the gaps among different approaches, we provide the MAE, RMSE, median, and 90-th percentile CDF in Fig. 16. The results indicate that by fine-tuning the GNN and FPDNN, it is possible to obtain 10% ~ 20% performance gain compared with zero-shot learning approaches. For example, the localization RMSE is 1.15 m for the zero-shot GNN and FPDNN, while the RMSE decreases to 1 m after fine-tuning. Nevertheless, the localization errors achieved by the zero-shot learning approaches are lower than the baselines.

By comparing Figs. 16(a) and 16(b), we can see that if we only have part of the environment information, there is a performance loss. If the GNN and FPDNN are trained with data samples obtained in the first four circles and tested with the data samples obtained in the last circle, the RMSE is 0.3 m



(a) Training with real-world data samples.

(b) Training with synthetic data samples, and fine-tuning with part of real-world data samples.

Fig. 16. Comparison of different methods.

(with GNN, FPDNN, and Kalman filter). If we train the GNN and FPDNN with the samples in green and test them with red samples, then the RMSE is 0.87 m (with GNN, FPDNN, and Kalman filter). This is because the green samples do not provide the environment information in the right part of the office.

F. Experimental Results in Different Scenarios

This part illustrates how to use our framework in unseen scenarios with no real-world data sample.

The synthetic data generator and our localization algorithm are pre-trained with real-world data samples in the office environment. In the other two scenarios, shopping mall and laboratory, we do not use real-world data samples to fine-tune the generator and localization algorithm. To improve localization accuracy, the synthetic data generator exploits the floor-plan images to generate synthetic data in the new scenarios. The newly generated data samples are used to fine-tune the localization algorithm. As there is no real-world data sample, this approach is also referred to as zero-shot learning.

As a baseline, we can also fine-tune the localization algorithm with real-world data samples in the new scenarios. Like Fig. 15(a), we fine-tune the GNN and FPDNN with one part of the samples and test them with the other part of the samples.

The MAE, RMSE, median, and 90-th percentile CDF obtained in the shopping mall are provided in Fig. 17(a). Specifically, the RMSE achieved by zero-shot learning with (or without) the Kalman filter is 1.33 m (or 1.19 m). After fine-tuning, the RMSE is reduced to 1.25 m (or 1.05 m). The performance gap is around 6.0% ~ 11.8%. We can observe similar performance gaps when using the other performance metrics. Nevertheless, the zero-shot learning approaches can reduce localization errors by around 31.1% ~ 55.4% compared with the hybrid RTT-RSS, Bayesian grid update, and CbT+WCCG models.

In Fig. 17(b), we estimate the localization errors in the laboratory. The performance gaps between zero-shot learning and fine-tuned approaches are around 7.0% ~ 16.8%. Zero-shot learning approaches can reduce the localization errors

by around 38.5% ~ 58.7% compared with the hybrid RTT-RSS, Bayesian grid update, and CbT+WCCG models. We note that in Fig. 17(b), the 90-th percentile CDFs achieved by the zero-shot learning (GNN+FPDNN+KF) and the fine-tuned approach are 1.55 m and 1.61 m, respectively. This is because we use the MSE as the loss function to fine-tune the GNN and FPDNN, and this may result in higher peak errors.

G. Multi-User Localization

This subsection evaluates our algorithm in multi-user scenarios, where $M = 2$ MDs are considered. In our testing, MD 1 is connected to all APs, and MD 2 is connected to two of the APs. We only provide the performance obtained by the zero-shot learning approaches in the shopping mall. The gaps between the zero-shot learning and other baselines are similar to the single-user scenarios. Similar to Section VII-F, we train the synthetic data generator in the office and use it to generate synthetic data samples in the shopping mall. The localization algorithm is only fine-tuned with the synthetic data samples, and real-world data samples in the shopping mall are only used for testing. For the laboratory scenario, there is no stable connection between the two MDs due to the blockages of walls and stairs. Thus, it is reduced to single-user localization. The testing samples of the two MDs are shown in Fig. 18.

The results are provided in Table III. With the existing baselines, we first estimate the location of MD 1 and then use it to estimate the location of MD 2. Thus, the estimation error of MD 1 is accumulated in the estimation error of MD 2. This issue may have more significant impacts on localization accuracy when there are more than two MDs. Specifically, with the trilateration method, the RMSE gap between MD 1 and MD 2 is 1.18 m. By using our GNN, we can obtain the estimated locations of the two MDs directly. With the GNN and Kalman filter, the RMSE gap between MD 1 and MD 2 is 0.53 m. This observation implies that our approach can alleviate the accumulation of estimate errors. In addition, compared with the localization accuracy in the single-user scenario in Fig. 17(a), MD 1 achieves lower localization errors in the multi-user scenario. For example, the RMSE of MD 1 is

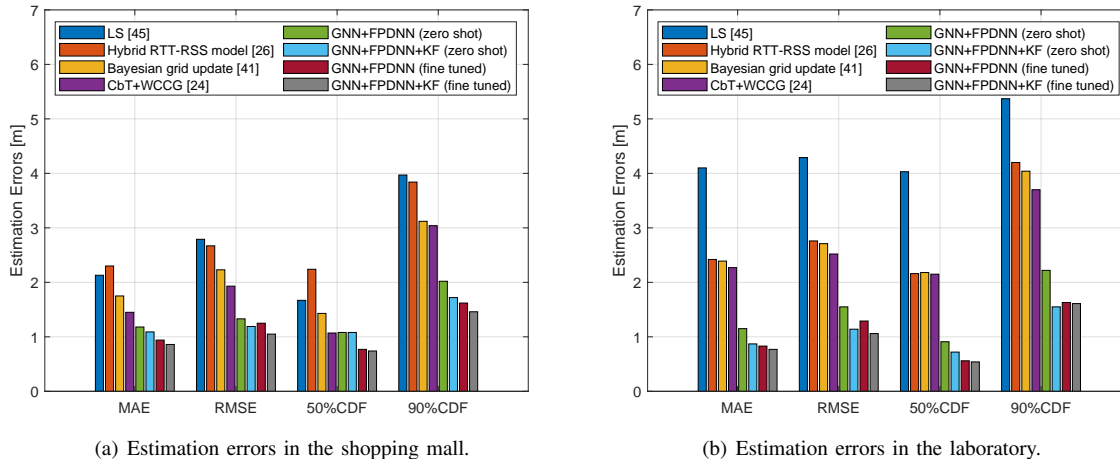


Fig. 17. Estimation errors of the proposed system and other baselines in different scenarios.

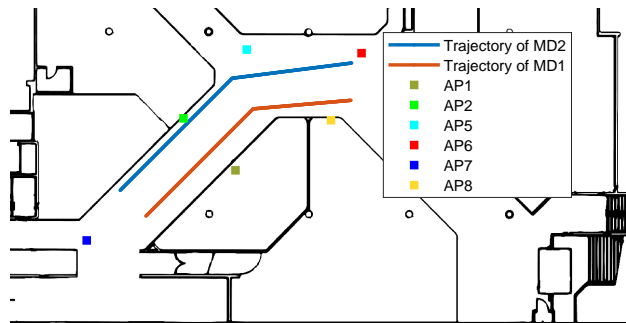


Fig. 18. Locations of two MDs and locations of six APs, where the MDs move along the trajectories.

TABLE III
ESTIMATION ERRORS IN THE SHOPPING MALL WITH TWO MDs

	Methods	MAE	RMSE	50% CDF	90% CDF
MD1	Trilateration	2.19	2.64	2.02	3.57
	With GNN	1.22	1.57	1.05	1.75
	With GNN+KF	1.03	1.23	0.92	1.71
	With GNN+FPDNN	0.9	1.08	0.78	1.65
	With GNN+FPDNN+KF	0.79	0.9	0.71	1.37
MD2	Trilateration	2.86	3.82	2.40	5.05
	With GNN	1.86	2.47	1.39	3.54
	With GNN+KF	1.42	1.76	1.19	2.52
	With GNN+FPDNN	1.77	2.39	1.28	3.52
	With GNN+FPDNN+KF	1.47	1.7	1.37	2.47

18.8% lower than the single-user scenario. This result indicates that the RTT and RSS information of MD 2 helps to improve the localization of MD 1 with our approach.

H. Complexity Analysis

Since the GNN and FPDNN are trained offline, the training complexity has no impact on the localization performance. We analyze the complexity of online inference. The number of on-device parameters and computational complexity, which are evaluated by the number of floating point operations (FLOPs) for processing one data sample of the proposed GNN and FPDNN, are provided in Table IV. It can be seen that the numbers of FLOPs and on-device parameters of the proposed GNN model are 2,704 and 1,381, respectively. For

TABLE IV
THE ON-DEVICE PARAMETERS AND COMPUTATIONAL COMPLEXITY FOR PROPOSED GNN AND FPDNN

	On-device computation (FLOPs)	On-device parameters
GNN	2,704	1,381
FPDNN	23,522,913	863,097

the proposed FPDNN, the numbers of FLOPs and on-device parameters are 23,522,913 and 863,097, respectively.

We evaluate the average computation time for inference using the GNN and FPDNN with the NVIDIA GeForce RTX 3090. The processing time of the GNN and FPDNN is 2 ms and 6 ms, respectively. The existing baselines require more computation time on the GPU than the CPU. This is because GPUs are optimized for specialized computations, such as deep learning. Thus, we evaluate their processing time on the Intel(R) Core(TM) i9-12900KF CPU. Specifically, the processing time of the hybrid RTT-RSS model, the Bayesian grid update method, and the CbT+WCCG method are 2.94 ms, 0.43 ms, and 26 ms, respectively. Compared with the minimum sampling interval between MDs and APs (200 ms), the processing time of all the localization algorithms is acceptable.

VIII. CONCLUSIONS

This paper proposed a multi-user indoor localization framework using floor-plan images, RTT distances, and RSS for localization. We first estimated the coarse locations of MDs by the GNN. Then, the positioning accuracy was further improved by the FPDNN. To improve the sample efficiency in real-world environments, we pre-trained the GNN and FPDNN with synthetic data samples generated in a virtual environment and tested them in different real-world environments, where no real-world data sample is available for training or fine-tuning the GNN and FPDNN. To collect data samples and validate our framework, we built a prototype, where the estimated locations of MDs are updated every 200 ms. Our experimental results showed that the proposed indoor localization system significantly outperforms the existing baseline methods in terms of localization errors. Specifically, the zero-shot learning

approaches can reduce localization errors by around 30% ~ 55% compared with three baselines from the existing literature.

REFERENCES

- [1] P. K. Enge, "The Global Positioning System: Signals, measurements, and performance," *Int. J. Wireless Inf. Networks*, vol. 1, pp. 83–105, 1994.
- [2] K. Ozsoy, A. Bozkurt, and I. Tekin, "Indoor positioning based on global positioning system signals," *Microwave Opt. Technol. Lett.*, vol. 55, no. 5, pp. 1091–1097, 2013.
- [3] X. Zhu, W. Qu, T. Qiu, L. Zhao, M. Atiquzzaman, and D. O. Wu, "Indoor Intelligent Fingerprint-Based Localization: Principles, Approaches and Challenges," *IEEE Commun. Surv. Tutorials*, vol. 22, no. 4, pp. 2634–2657, 2020.
- [4] F. Zafari, A. Gkelias, and K. K. Leung, "A Survey of Indoor Localization Systems and Technologies," *IEEE Commun. Surv. Tutorials*, vol. 21, no. 3, pp. 2568–2599, 2019.
- [5] S. He and S.-H. G. Chan, "Wi-Fi Fingerprint-Based Indoor Positioning: Recent Advances and Comparisons," *IEEE Commun. Surv. Tutorials*, vol. 18, no. 1, pp. 466–490, 2016.
- [6] Z. Jianyong, L. Haiyong, C. Zili, and L. Zhaohui, "RSSI based Bluetooth Low Energy Indoor Positioning," in *Proc. IEEE Int. Conf. Indoor Positioning Indoor Navig. (IPIN)*, 2014, pp. 526–533.
- [7] S. S. Saab and Z. S. Nakad, "A Standalone RFID Indoor Positioning System Using Passive Tags," *IEEE Trans. Ind. Electron.*, vol. 58, no. 5, pp. 1961–1970, 2011.
- [8] C. Zhang and X. Zhang, "LiTell: Robust Indoor Localization Using Unmodified Light Fixtures," in *Proc. ACM Int. Conf. Mobile Comput. Networking (MOBICOM)*, 2016, pp. 230–242.
- [9] M. Werner, M. Kessel, and C. Marouane, "Indoor positioning using smartphone camera," in *Proc. IEEE Int. Conf. Indoor Positioning Indoor Navig. (IPIN)*, 2011, pp. 1–6.
- [10] Z. Ma, S. Poslad, S. Hu, and X. Zhang, "A fast path matching algorithm for indoor positioning systems using magnetic field measurements," in *Proc. IEEE 28th Annu. Int. Symp. Pers. Indoor, Mobile Radio Commun. (PIMRC)*, 2017, pp. 1–5.
- [11] C. Ma, C. Wan, Y. W. Chau, S. M. Kang, and D. R. Selviah, "Subway Station Real-time Indoor Positioning System for Cell Phones," in *Proc. Int. Conf. Indoor Positioning Indoor Navig. (IPIN)*, 2017, pp. 1–7.
- [12] Z. Ma, J. Bigham, S. Poslad, B. Wu, X. Zhang, and E. Bodanese, "Device-Free, Activity During Daily Life, Recognition Using a Low-Cost Lidar," in *Proc. IEEE Global Commun. Conf. (GLOBECOM)*, 2018, pp. 1–6.
- [13] X. Li *et al.*, "A Cooperative Relative Localization System for Distributed Multi-Agent Networks," *IEEE Trans. Veh. Technol.*, pp. 1–16, 2023.
- [14] S. u. Rahman, S. Ullah, and S. Ullah, "A Mobile Camera Based Navigation System for Visually Impaired People," in *Proc. ACM 7th Int. Conf. on Commu. Broadband Networking (ICCBN)*, 2019, pp. 63–66.
- [15] G. Glanzer, T. Bernoulli, T. Wiessflecker, and U. Walder, "Semi-autonomous Indoor Positioning Using MEMS-based Inertial Measurement Units and Building Information," in *Proc. 6th Workshop on Positioning, Navig. and Commun. (WPNC)*, 2009, pp. 135–139.
- [16] Y. Yu, R. Chen, L. Chen, W. Li, Y. Wu, and H. Zhou, "Autonomous 3D Indoor Localization Based on Crowdsourced Wi-Fi Fingerprinting and MEMS Sensors," *IEEE Sens. J.*, vol. 22, no. 6, pp. 5248–5259, 2022.
- [17] Samsung S24 ultra. Accessed: Mar. 2024. [Online]. Available: <https://www.samsung.com/au/smartphones/galaxy-s24-ultra/>
- [18] Google Pixel 8 Pro. Accessed: Mar. 2024. [Online]. Available: https://store.google.com/au/product/pixel_8_pro
- [19] N. Singh, S. Choe, and R. Punmiya, "Machine Learning Based Indoor Localization Using Wi-Fi RSSI Fingerprints: An Overview," *IEEE Access*, vol. 9, pp. 127 150–127 174, 2021.
- [20] C. Basri and A. El Khadimi, "Survey on Indoor localization System and Recent Advances of WiFi Fingerprinting Technique," in *Proc. IEEE Int. Conf. Multimedia Comput. Syst. (ICMCS)*, 2016, pp. 253–259.
- [21] C. Zhou, J. Liu, M. Sheng, Y. Zheng, and J. Li, "Exploiting Fingerprint Correlation for Fingerprint-Based Indoor Localization: A Deep Learning Based Approach," *IEEE Trans. Veh. Technol.*, vol. 70, no. 6, pp. 5762–5774, 2021.
- [22] M. Ibrahim *et al.*, "Verification: Accuracy Evaluation of WiFi Fine Time Measurements on an Open Platform," in *Proc. ACM Int. Conf. on Mobile Comput. and Networking (MOBICOM)*, 2018, pp. 417–427.
- [23] C. Gentner, M. Ulmschneider, I. Kuehner, and A. Dammann, "Wi-Fi-RTT Indoor Positioning," in *Proc. IEEE Symp. Position Locat. Navig. (PLANS)*, 2020, pp. 1029–1035.
- [24] C. Ma, B. Wu, S. Poslad, and D. R. Selviah, "Wi-Fi RTT Ranging Performance Characterization and Positioning System Design," *IEEE Trans. Mob. Comput.*, vol. 21, no. 2, pp. 740–756, 2022.
- [25] I. Martin-Escalona and E. Zola, "Ranging Estimation Error in WiFi Devices Running IEEE 802.11mc," in *Proc. IEEE Conf. Global Commun. (GLOBECOM)*, 2020, pp. 1–7.
- [26] G. Guo, R. Chen, F. Ye, X. Peng, Z. Liu, and Y. Pan, "Indoor Smartphone Localization: A Hybrid WiFi RTT-RSS Ranging Approach," *IEEE Access*, vol. 7, pp. 176 767–176 781, 2019.
- [27] N. Dvorecki, O. Bar-Shalom, L. Banin, and Y. Amizur, "A Machine Learning Approach for Wi-Fi RTT Ranging," in *Proc. Int. Tech. Meet. Inst. Navig.*, 2019, pp. 435–444.
- [28] Y. Wang, K. Gu, Y. Wu, W. Dai, and Y. Shen, "NLOS Effect Mitigation via Spatial Geometry Exploitation in Cooperative Localization," *IEEE Trans. Wireless Commun.*, vol. 19, no. 9, pp. 6037–6049, 2020.
- [29] L. Huang *et al.*, "HPIPS: A High-Precision Indoor Pedestrian Positioning System Fusing Wi-Fi-RTT, MEMS, and Map Information," *Sensors*, vol. 20, no. 23, p. 6795, 2020.
- [30] H. Cao, Y. Wang, and J. Bi, "Smartphones: 3D Indoor Localization Using Wi-Fi RTT," *IEEE Commun. Lett.*, vol. 25, no. 4, pp. 1201–1205, 2021.
- [31] M. Si, Y. Wang, S. Xu, M. Sun, and H. Cao, "A Wi-Fi FTM-Based Indoor Positioning Method with LOS/NLOS Identification," *Appl. Sci.*, vol. 10, no. 3, p. 956, 2020.
- [32] H. Cao, Y. Wang, J. Bi, S. Xu, M. Si, and H. Qi, "Indoor Positioning Method Using WiFi RTT Based on LOS Identification and Range Calibration," *ISPRS Int. J. of Geo-Inf.*, vol. 9, no. 11, p. 627, 2020.
- [33] K. Han, S. M. Yu, and S.-L. Kim, "Smartphone-based Indoor Localization Using Wi-Fi Fine Timing Measurement," in *Proc. IEEE Int. Conf. Indoor Positioning Indoor Navig. (IPIN)*, 2019, pp. 1–5.
- [34] K. Bregar and M. Mohorčič, "Improving Indoor Localization Using Convolutional Neural Networks on Computationally Restricted Devices," *IEEE Access*, vol. 6, pp. 17 429–17 441, 2018.
- [35] Y. Dong, T. Arslan, and Y. Yang, "Real-Time NLOS/LOS Identification for Smartphone-Based Indoor Positioning Systems Using WiFi RTT and RSS," *IEEE Sens. J.*, vol. 22, no. 6, pp. 5199–5209, 2021.
- [36] J. Choi, "Enhanced Wi-Fi RTT Ranging: A Sensor-Aided Learning Approach," *IEEE Trans. Veh. Technol.*, vol. 71, no. 4, pp. 4428–4437, 2022.
- [37] Y. Li, S. Mazuelas, and Y. Shen, "A Variational Learning Approach for Concurrent Distance Estimation and Environmental Identification," *IEEE Trans. Wireless Commun.*, vol. 22, no. 9, pp. 6252–6266, 2023.
- [38] J.-H. Seong, S.-H. Lee, W.-Y. Kim, and D.-H. Seo, "High-Precision RTT-Based Indoor Positioning System Using RCDN and RPN," *Sensors*, vol. 21, no. 11, p. 3701, 2021.
- [39] G. Guo, R. Chen, X. Niu, K. Yan, S. Xu, and L. Chen, "Factor Graph Framework for Smartphone Indoor Localization: Integrating Data-Driven PDR and Wi-Fi RTT/RSS Ranging," *IEEE Sens. J.*, vol. 23, no. 11, pp. 12 346–12 354, 2023.
- [40] L. Zehua, S. Junna, and Y. Ziyang, "Indoor Integrated Navigation on PDR/Wi-Fi/barometer via Factor Graph with Local Attention," *IEEE Sens. J.*, pp. 1–1, 2023.
- [41] B. Horn, "Indoor Localization Using Uncooperative Wi-Fi Access Points," *Sensors*, vol. 22, no. 8, p. 3091, 2022.
- [42] A. Dosovitskiy *et al.*, "An Image is Worth 16x16 Words: Transformers for Image Recognition at Scale," 2021, *arXiv:2010.11929*. [Online]. Available: <https://arxiv.org/abs/2010.11929>
- [43] D. Zhou *et al.*, "DeepViT: Towards Deeper Vision Transformer," 2021, *arXiv:2103.11886*. [Online]. Available: <https://arxiv.org/abs/2103.11886>
- [44] L. Bottou, "Large-Scale Machine Learning with Stochastic Gradient Descent," in *Proc. Int. Conf. Comput. Stat. (COMPSTAT)*, 2010, pp. 177–186.
- [45] I. Guven, C.-C. Chong, and F. Watanabe, "Analysis of a Linear Least-Squares Localization Technique in LOS and NLOS Environments," in *Proc. IEEE Veh. Technol. Conf. (VTC)*, 2007, pp. 1886–1890.
- [46] M. Lecci, P. Testolina, M. Polese, M. Giordani, and M. Zorzi, "Accuracy Versus Complexity for mmWave Ray-Tracing: A Full Stack Perspective," *IEEE Trans. Wirel. Commun.*, vol. 20, no. 12, pp. 7826–7841, 2021.
- [47] D. P. Kingma and J. Ba, "Adam: A Method for Stochastic Optimization," 2014, *arXiv:1412.6980*. [Online]. Available: <https://arxiv.org/abs/1412.6980>